

A peer-reviewed version of this preprint was published in PeerJ on 16 October 2019.

[View the peer-reviewed version](https://doi.org/10.7717/peerj.7875) (peerj.com/articles/7875), which is the preferred citable publication unless you specifically need to cite this preprint.

Barbi M, Bell PR, Fanti F, Dynes JJ, Kolaceke A, Buttigieg J, Coulson IM, Currie PJ. 2019. Integumentary structure and composition in an exceptionally well-preserved hadrosaur (Dinosauria: Ornithischia) PeerJ 7:e7875 <https://doi.org/10.7717/peerj.7875>

Integumentary structure and composition in an exceptionally well-preserved hadrosaur (Dinosauria: Ornithischia)

Mauricio Barbi¹ Corresp., Equal first author, **Phil R. Bell**² Equal first author, **Federico Fanti**^{3,4}, **James J. Dynes**⁵, **Anezka Kolaceke**¹, **Josef Buttigieg**⁶, **Philip J. Currie**⁷

¹ Physics Department, University of Regina, Regina, Saskatchewan, Canada

² School of Environmental and Rural Science, University of New England, Armidale, New South Wales, Australia

³ Dipartimento di Scienze Biologiche, Geologiche e Ambientali, Alma Mater Studiorum, University of Bologna, Bologna, Italy

⁴ Museo Geologico Giovanni Capellini, University of Bologna, Bologna, Italy

⁵ Canadian Light Source Inc., University of Saskatchewan, Saskatoon, Saskatchewan, Canada

⁶ Department of Biology, University of Regina, Regina, Saskatchewan, Canada

⁷ Biological Sciences, University of Alberta, Edmonton, Alberta, Canada

Corresponding Author: Mauricio Barbi

Email address: barbi@uregina.ca

Preserved labile tissues (e.g. skin, muscle) in the fossil record of terrestrial vertebrates are increasingly becoming recognized as an important source of biological and taphonomic information. Here, we combine a variety of synchrotron radiation techniques with scanning electron and optical microscopes to elucidate the structure of 72 million-year-old squamous (scaly) skin associated with a hadrosaurid dinosaur from the Late Cretaceous of Alberta, Canada. Scanning electron and optical microscopy independently reveal that the three-dimensionally preserved scales are associated with a band of carbon-rich layers up to a total thickness of 75 μm . Compositionally, this band deviates from that of the surrounding matrix; Fourier-transform infrared spectroscopy and soft X-ray spectromicroscopy analyses indicate the presence of carboxylic compounds. The regions corresponding to the integumentary layers are distinctively enriched in iron compared to the associated sedimentary matrix and seem associated to kaolinite. These carbonyl-rich layers are apparently composed of subcircular bodies resembling preserved cell structures. Each of these structures is encapsulated by calcite/vaterite, with iron predominantly concentrated at its center. The presence of iron, calcite/vaterite and kaolinite might have played important roles in the preservation of the layered structures.

Integumentary structure and composition in an exceptionally well-preserved hadrosaur (Dinosauria: Ornithischia)

Mauricio Barbi¹, Phil R. Bell², Federico Fanti^{3,4}, James J. Dynes⁵, Anezka Kolaceke¹, Josef Buttigieg⁶, and Philip J. Currie⁷

¹Department of Physics, University of Regina, Regina, Saskatchewan, Canada

²School of Environmental and Rural Science, University of New England, Armidale, New South Wales, Australia

³Museo Geologico Giovanni Capellini, Università di Bologna, Bologna, Italy

⁴Dipartimento di Scienze Biologiche, Geologiche e Ambientali, Alma Mater Studiorum, Università di Bologna, Bologna, Italy

⁵Canadian Light Source Inc., University of Saskatchewan, Saskatoon, Saskatchewan, Canada

⁶Department of Biology, University of Regina, Regina, Saskatchewan, Canada

⁷Biological Sciences, University of Alberta, Edmonton, Alberta, Canada

Corresponding author:

Mauricio Barbi¹

Email address: barbi@uregina.ca

ABSTRACT

Preserved labile tissues (e.g. skin, muscle) in the fossil record of terrestrial vertebrates are increasingly becoming recognized as an important source of biological and taphonomic information. Here, we combine a variety of synchrotron radiation techniques with scanning electron and optical microscopes to elucidate the structure of 72 million-year-old squamous (scaly) skin associated with a hadrosaurid dinosaur from the Late Cretaceous of Alberta, Canada. Scanning electron and optical microscopy independently reveal that the three-dimensionally preserved scales are associated with a band of carbon-rich layers up to a total thickness of 75 μm . Compositionally, this band deviates from that of the surrounding matrix; Fourier-transform infrared spectroscopy and soft X-ray spectromicroscopy analyses indicate the presence of carboxylic compounds. The regions corresponding to the integumentary layers are distinctively enriched in iron compared to the associated sedimentary matrix and seem associated to kaolinite. These carbonyl-rich layers are apparently composed of subcircular bodies resembling preserved cell structures. Each of these structures is encapsulated by calcite/vaterite, with iron predominantly concentrated at its center. The presence of iron, calcite/vaterite and kaolinite might have played important roles in the preservation of the layered structures.

INTRODUCTION

Fossilized dinosaur integument has been known for nearly 150 years, yet it is only recently that it has been considered more than a simple impression (i.e. trace fossil) of the original skin surface (Sternberg, 1953; Martill, 1991; Kellner, 1996). Although feathers and filamentary "protofeathers" of avian and non-avian theropods have received considerable attention, particularly in the past two decades, squamous (scaly) skin is more widespread and was probably plesiomorphic for Dinosauria (Barrett et al., 2015).

Significant advances in our understanding of the preservation and structure of squamous skin have been achieved with the use of synchrotron radiation techniques (Barbi et al., 2014, and references therein). Notably, it is now generally accepted that labile tissues, such as skin and muscle, can preserve and remain intact millions of years after the death of the organism (Schweitzer et al., 2005; Lingham-Soliar, 2008; Manning et al., 2009; Li et al., 2010; Zhang et al., 2010; Li et al., 2012; Lindgren et al., 2014; Bertazzo et al., 2015; Lindgren et al., 2018).

Although hadrosaur skin is relatively common in the fossil record (Davis, 2014; Bell, 2014), few studies have investigated either its composition or the possible determining factors behind its preservation (e.g. Manning et al., 2009). We present a qualitative study of three-dimensionally preserved squamous skin (herein referred to simply as skin) from a hadrosaurid dinosaur from the Upper Cretaceous (Campanian) Wapiti Formation discovered near the city of Grande Prairie, Alberta, Canada. In this study, potential preserved structures that might be related to the original skin are investigated using a systematic approach employing scanning electron and optical microscopy, and an array of synchrotron radiation techniques.

SPECIMEN AND GEOLOGICAL SETTING

UALVP 53290 represents an incomplete articulated-to-associated hadrosaurid skeleton comprising most of the thoracic region, forelimb and pelvic elements (Fig. 1). Parts of the tail likely continue into the cliff but could not be recovered owing to the precipitous nature of the outcrop. The only cranial element found, an incomplete jugal, indicates hadrosaurine affinities (triangular, asymmetrical anterior process; Horner et al., 2004); however, a second and more complete skeleton (UALVP 53722) found several hundred meters upstream of and approximately 10 m stratigraphically above UALVP 53290 is identifiable as *Edmontosaurus regalis* (Bell et al. 2014). As *E. regalis* is the sole hadrosaurine known from this stratigraphic interval (Bell and Campione, 2014), we tentatively refer UALVP 53290 to *Edmontosaurus cf. regalis*. Sheets of displaced fossilized integument were found close to the forelimbs of UALVP 53290 (Fig. 1A) and occur in two types: 1) as a 2 mm thick black rind preserving the three-dimensionality of the epidermal scales (Fig. 1B); and 2) as low-relief structures covered in a thin, oxide-rich patina (Fig. 1C). The skin samples examined here were slightly displaced relative to their true life position but are presumed to have come from the dorsal (anterior) surface of the forearm. The integument is composed of large (10 mm), hexagonal basement scales (*sensu* Bell (2012); type '1' according to the above descriptions) identical to scales on the upper surface of the forearm in other *Edmontosaurus* specimens (Osborn, 1912; Manning et al., 2009).

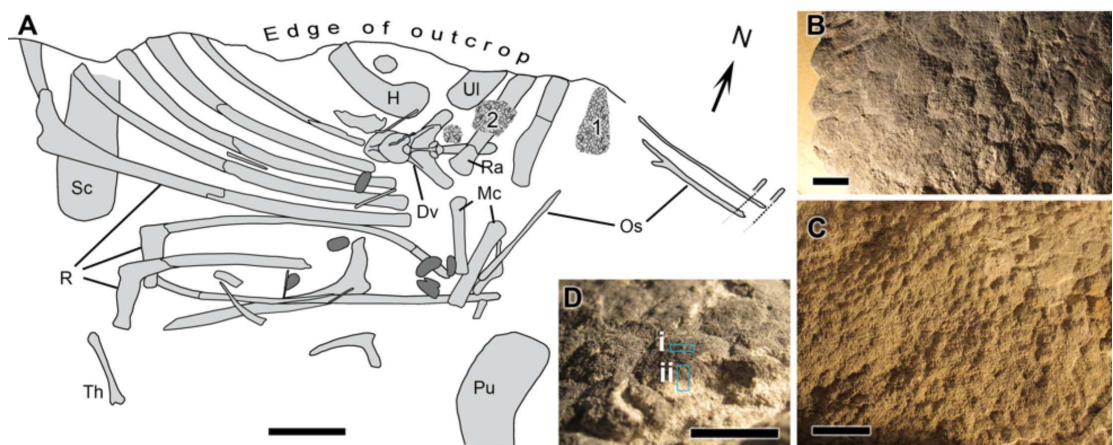


Figure 1. *Edmontosaurus cf. regalis* (UALVP 53290). (A) quarry map showing location of preserved integument (indicated by numerals) shown in (B) and (C). Dark grey regions are freshwater bivalves. (B) Close up of 1 showing dark-coloured polygonal scales (type "1" preservation; see text). (C) Close up of 2 showing cluster areas associated with the forearm integument. (D) Detail of dark type "1" scales in oblique view showing sampling locations for spectromicroscopy: samples were collected with a microtome from (i) the outer surface of the epidermal scale to produce a light-coloured powder, and (ii) from a cross section of the scale that penetrated into the pale underlying matrix to produce a dark-coloured powder. Scale bar in (A) is 10 cm. Scale bars in (B)–(D) are 1 cm. Abbreviations: Dv, dorsal vertebra; H, humerus; Mc, metacarpal; Os, ossified tendon; Pu, pubis; R, rib; Sc, scapula; Th, theropod tibia; Ul, ulna.

UALVP 53290 comes from the Upper Cretaceous deposits of the Wapiti Formation exposed near the city of Grande Prairie in west-central Alberta, western Canada. The specimen was collected at the Red Willow Falls locality, less than one kilometer to the east of the Alberta-British Columbia border.

From a taphonomic perspective, the specimen comes from an undescribed monodominant hadrosaurine bonebed (*sensu* Eberth et al. (2007)), characterized by articulated-to-disarticulated elements of at least five individuals. Because exposures are on steep, sometimes overhanging cliffs, skeletal remains (including UALVP 53290 discussed here) are usually recovered in blocks derived from rock falls rendering precise mapping (including orientations, skeletal completeness and associations between individuals) virtually impossible. In this area, upper Campanian deposits of the Wapiti Formation have been dated at 72.58 ± 0.09 Ma (Bell, 2014) and consist of repeating fining-upward sequences of crevasse-splays, muddy and organic-rich overbank deposits, and minor sandy channel fills. Sandstones are primarily formed by poorly-sorted quartz, feldspar, and carbonate clasts, commonly presenting a carbonatic cement. Thin and discontinuous altered volcanic ash beds are found at the top of fining-upward successions, where they are locally interbedded with coal lenses (see also Fanti (2009)). Overall stacking pattern, facies distribution, and abundant megaplant material are indicative of a braided channel belt within a fluvial plain, characterized by high-water tables, poorly-drained soils, and abundant vegetation (Bell et al., 2013, 2014).

Paleogeographic reconstruction for the Campanian places the Red Willow Falls beds at approximately 400 Km north-west from the coeval paleoshoreline (Fanti and Catuneanu, 2009, 2010), and at a paleolatitude of approximately 65° N (Fanti and Miyashita, 2009, and references therein). Therefore, depositional conditions at the Red Willow Falls locality are unequivocally representative of terrestrial, freshwater conditions in a high-latitude setting.

In addition to the hadrosaur described here, this locality has yielded abundant cranial and postcranial hadrosaur elements referable to *Edmontosaurus regalis*, as well as isolated theropod (tyrannosaurid) teeth, diverse vertebrate tracks, and larval mayfly body fossils (Bell et al., 2013, 2014; Fanti et al., 2013; Bell and Campione, 2014).

MATERIALS AND METHODS

All fieldwork to collect UALVP 53290 was done with Palaeontological Collecting Permits issued by the Historical Resources Division (through the Royal Tyrrell Museum of Palaeontology) of the Government of Alberta, Canada. The permit to excavate Palaeontological Resources for the Grande Prairie area, file number 3950-605, was issued to Philip J. Currie, University of Alberta.

General Strategy

As an overall strategy, Scanning Electron Microscopy (SEM) elemental maps of the skin were first derived to investigate possible markers that could (a) discriminate the skin from the matrix, and (b) identify potential regions for the presence of organic contents. Subsequently, the chemical states of a series of elements were identified using X-ray methods, along with analyses using Fourier Transform Infrared Spectroscopy (FTIR).

SEM studies of a $20 \mu\text{m}$ thick cross section of the hadrosaur skin were conducted with the intentions listed. The thin section covers the first 2 cm of the sample starting from the outer surface of the scales (see section *Sample Preparation*). Characteristic X-ray lines, generated in processes involving the interactions between the electron beam and atoms in the sample, were used to produce elemental maps covering a $100 \mu\text{m}$ thick region spanning from the outer surface to the deepest regions of the sample, and single-point spectral measurements (see section *Results* for details).

Based on these observations, some samples of the skin (at least $100 \mu\text{m}$ thick and incorporating the outer surface of the scales) were tested at different beamline endstations at the Canadian Light Source (CLS), Saskatoon, Canada, using synchrotron radiation techniques. Only the data from two techniques are included in this paper, corresponding to Fourier Transform Infrared (FTIR) spectroscopy and X-ray Near Edge Spectroscopy (XANES). FTIR and XANES were used to probe for complex compounds and the chemical state of certain elements of interest, respectively. An elemental map using X-ray fluorescence techniques is included in the supplemental material (section 1).

Sample Preparation

Small ($\sim 1 \text{ cm}^2$) sections of pristine skin were sampled from the hadrosaur forearm during excavation to avoid contact with potential contaminants (anthropogenic or otherwise). All analytical samples were prepared from a single pristine skin sample.

For measurements using scanning electron microscopy, a 20 μm section was manufactured¹ using standard petrographic thin section preparation techniques. Carbon was used to coat the sample (under high vacuum conditions) to improve conductivity before the SEM measurements. A small carbon signal is, then, expected in all spectra collected with this technique. Any excess carbon observed is assumed to be endogenous to the sample.

The CLS Mid-Infrared (MidIR) beamline endstation (May et al., 2007) was used for the FTIR measurements. Three different samples were prepared. Two of these were sampled from a pristine piece of the dinosaur skin embedded in matrix. A microtome (Microtome, Leica EM UC7) with a diamond blade was used to "scrape" one of the scales on two different surfaces (Fig. 1d): 1. on the outer (superficial) surface of the scale, producing a light-coloured powder (hereafter called "light-coloured powder"), and; 2. on the broken cross-section of the scale and incorporating some of the underlying matrix, producing a dark-coloured powder (hereafter called "dark-coloured powder"). The third sample, also a small pristine piece of skin still embedded in matrix, was immersed in HCl for two days to remove most of its mineral contents. The remaining sample was then washed with ethanol and air-dried at room temperature.

For XANES analysis, a piece of hadrosaur skin and the attached matrix was sectioned at 100 nm into a water bath (Microtome, Leica EM UC7). Due to the hardness of the sample, only flakes of the sample, containing skin and debris from the sediment, were obtained. The flakes and sediment were removed from the water bath and deposited onto a silicon nitride membrane, air-dried at room temperature and examined using X-ray spectromicroscopy with the Spectromicroscopy (SM) (Kaznatcheev et al., 2007) beamline endstation.

Instrumentation

For the SEM measurements, the sample was subjected to high vacuum. To determine the best operational conditions, several areas were imaged at a range of beam currents (varied by increasing or decreasing the beam spot size), utilizing a smaller beam aperture and variable kV. Optimum conditions that provided the clearest and sharpest images at high magnification, but that did not lead to sample charging or sample degradation, were found to be 10-15 kV and a spot size of 65-70 μm . Examinations of samples were undertaken with both the secondary electron (SEI), and back-scattered electron (BSE) detectors fitted to the Jeol instrument.

For FTIR measurements, the MidIR beamline provides a beam in the mid infrared region produced by a bending magnet, covering an energy range of 0.070-0.744 eV. A Hyperion 3000 IR microscope, cooled with liquid nitrogen, was used with the top objective set to 0.45 and the bottom objective set to 0.30, resulting in a beam spot size of 20 μm . 128 scans in transmission mode were performed per measured point. The data was processed using the Bruker commercial software package OPUS² (baseline corrections were applied as provided with the software).

The scanning transmission X-ray microscope (STXM) endstation on the SM beamline (10ID-1) was used to collect all X-ray imagery and spectroscopy. Image sequences (i.e., stacks) (Dynes et al., 2006b) were collected at the C, Mg, Al and Si K-edges and at the K, Ca and Fe L-edges. The as-measured transmitted signatures (I) were converted to optical density (absorbance = OD = $-\ln(I/I_0)$) using the incident flux (I_0) measured through areas where there was no sample present. The stacks (dimensions 8 x 8 μm) were collected at a spatial resolution of 60 nm and a dwell time of 1 ms/pixel. Principal component and cluster analysis (PCA-CA) was used to determine the number of chemical components present and/or derive spectra in selected image sequences (Lerotic et al., 2004). Quantitative maps from the image sequences were obtained using singular value decomposition (SVD) to fit the spectrum at each pixel to a linear combination of reference spectra of the components suspected to be present, or using spectra derived from the image sequence (Dynes et al., 2006a). Representative spectra were derived from the component maps using threshold masking. Axis2000³ was used for all STXM data processing.

The Very Sensitive Elemental and Structural Probe Employing Radiation from a Synchrotron (VES-PERS) CLS beamline endstation (McIntyre et al., 2010) was also used to investigate possible chemical markers differentiating the skin from its associated sedimentary matrix. X-ray fluorescence spectroscopy using a polychromatic beam with energy ranging from 6 keV to 30 keV was employed, covering elements such as Ti, Ca, Mn, Fe, Zn, Sr, Y and Zr, among several others. The results of these measurements for Fe,

¹ Vancouver Petrographics, Langley, British Columbia, Canada

² <https://www.bruker.com/products/infrared-near-infrared-and-raman-spectroscopy/opus-spectroscopy-software.html>

³ Hitchcock, A. P., aXis2000, <http://unicorn.mcmaster.ca/aXis2000.html>

Ca, Cu and Mn are presented with the supplemental material.

RESULTS

Initial elemental mapping using the VESPERs beamline (supplemental material, Fig. S1) shows that the skin is enriched in Fe compared to the surrounding matrix. In what follows, further results from measurements using SEM and SR techniques along with optical images are presented.

Scanning Electron Microscopy (SEM) Analysis

Back-scattered electron (BSE) SEM imagery of a thin section comprising both skin and associated matrix was used to identify concentrations of lower atomic number (low Z) elements (dark regions in Figs. 2C,D) and higher-Z elements (brighter areas in Figs. 2C,D). Thus, carbon-based structures (low Z), if present, are expected in the darker areas, while sedimentary material (high Z) will be mostly localized in brighter areas. SEM images show that, in general, the entire sample is dominated by angular particles of a sedimentary nature (white-to-grey in Figs. 2C,D). In contrast, the outermost 50–75 μm differs in both texture and concentration of elements. BSE SEM shows an outermost layer of white (high-Z; $\sim 25 \mu\text{m}$ thick) material identified as barite (supplemental material, section 2) that caps a region of numerous thin, dark bands (low Z) up to a total thickness of $\sim 35\text{--}75 \mu\text{m}$. The dark bands are interrupted by discontinuous laminae, or lenses, of higher Z material (grey in Fig. 2C).

To partially assess the elemental compositions of the light and dark bands, a number of spectral distributions (using X-ray emission spectroscopy) were collected at different points on the sample as depicted in Fig. 2C. Most of these points (points 1 and 3–6 in Fig. 2C) were from grey or white areas (all high Z) identified by BSE SEM. Unsurprisingly, they showed no particular characteristic indicating contribution of organic components to each respective spectrum (supplemental material, section 2). The most interesting spectrum comes from a region corresponding to lower-Z elements (point 2 in Fig. 2C and darker region indicated by an arrow in Fig. 2D). Fig. 3 depicts this spectrum and is typical of all similar low Z areas distributed in the sample. These dark, carbon-rich areas are restricted to the outer parts of the sample and, in most cases, are covered with layers of kaolinite (among other minerals such as quartz; point 5 in Fig. 2C; see also supplemental material). Interestingly, kaolinite seems to be mostly concentrated around these darker areas, which might indicate a correlation between carbon and kaolinite during diagenesis.

An elemental map of an area containing both high and low-Z regions (sedimentary and carbon-rich regions, respectively) was achieved using SEM X-ray in emission mode at a 5 μm scale. Optical imaging (Fig. 4A) of the carbon-rich (low Z) region confirms the identification of discrete layers or bands (dark structures in Fig. 4A). However, the SEM images alone are not sufficient to resolve those structures due to the two-dimensional nature of the measurement technique. Carbon distribution is directly correlated to the darker area in the sample (Fig. 4B), whereas oxygen, aluminum and silica are mostly concentrated outside the carbon-rich region (Figs. 4C, 4D and 4E, respectively).

Measurements with the MidIR Beamline Endstation

The first measurements using the MidIR beamline were carried out using the sample cleaned with HCl. This technique served to remove the hardest mineral parts from the sample leaving only a small amount of material associated with the epidermal scale. Most of this remaining material is identified as kaolinite (in agreement with the SEM results; supplemental material, section 2), which is characterized by peaks at 3690, 3651, 3619, 1113, 1026, 1005, 936, and 910 cm^{-1} (Fig. 5).

The peak at 1635 cm^{-1} is likely related to the presence of montmorillonite (a type of smectite) and arises from the bending vibration of the OH group. The spectrum of montmorillonite has several peaks that superimpose with some others from kaolinite, although the peak at $\sim 1635 \text{ cm}^{-1}$ is strictly characteristic of the smectite group. On the other hand, the broad peak centered at $\sim 3400 \text{ cm}^{-1}$ is likely due to O-H stretch vibrations, which may be indicative of water impurities in the sample. If that is true, O-H scissoring vibrational excitations could also explain the peak at $\sim 1635 \text{ cm}^{-1}$. Another possibility could be contamination by alcohol (used to clean the glass slides that hold the samples); however, the absence of other peaks characteristic of the alcohol group refutes this supposition.

Interestingly, the peaks located at $\sim 2922 \text{ cm}^{-1}$ and $\sim 2849 \text{ cm}^{-1}$ are likely the result of C-H vibrations and could provide evidence for the presence of organic material in the sample. The peak at $\sim 1635 \text{ cm}^{-1}$ could support this statement as it can be associated to the presence of amide-1 (indicative of carboxylic

acid in the sample); however, as discussed above, this peak is likely of inorganic nature. Thus, the absence of other peaks that could support the presence of, for example, some carbonyl groups does not support the interpretation of an organic origin for those two peaks around 2900 cm^{-1} . Another plausible explanation for the appearance of those peaks is that they arise from C-O vibrations in carbonates. However, the complete absence of any significant peak near 1400 cm^{-1} (characteristic of carbonates) makes this a weak proposition.

The potential contamination by water absorption makes the above sample unsuitable for searching for organic material. The peaks arising from vibrational excitations of water molecules can superimpose those produced by vibrational modes in organic groups, making identification of the latter difficult.

Several maps and spectra were also collected from both the light and dark-coloured powder samples with the MidIR beamline using FTIR in transmission mode. The sample preparation in this case was less invasive (from a chemical perspective) and required less manipulation. While the light-coloured powder sample yielded spectra rich in mineral signatures (supplemental material, section 4), such as kaolinite and montmorillonite, the dark-coloured powder provided a more intriguing selection of spectra.

Four spectra (Fig. 7) were selected from the map shown in Fig. 6 based on the features present in one or more of the areas of interest (the complete set of spectra can be found in the supplemental material, Fig. S7). While some minerals can be associated with some of the observed peaks, there are other peaks that likely indicate the presence of organic traces (Table 1).

Peak Position	Possible Association
1610 cm^{-1}	Carboxylic acid, COO anti-symmetric stretch.
1680 cm^{-1}	Carbonyl, C-O stretch α,β -unsaturated aldehydes and ketones; alkene, C-C stretch.
1789 cm^{-1} and 1869 cm^{-1}	Anhydrides acid, C-O symmetric stretch and C-O asymmetric stretch, respectively.
2514 cm^{-1}	Calcite; Dolomite with calcite phase.
2849 cm^{-1} and 2964 cm^{-1}	Aliphatic compounds (alkenes), C-H vibrations.

Table 1. Associations between peaks in Fig. 7 and possible compounds.

In particular, the appearance of the 1789 cm^{-1} and 1869 cm^{-1} peaks in a FTIR spectrum is indicative of the presence of anhydrides acid (Coates, 2000). Interestingly, this acid is produced from the dehydration of carboxylic acids. In this case, the peak at 1789 cm^{-1} would correspond to C-O symmetric stretch while that at 1869 cm^{-1} would correspond to C-O asymmetric stretch.

Measurements using the SM Beamline Endstation

To further constrain the possible explanations for the observations described here, data were collected using the SM beamline from samples produced using a microtome. Optical images of the sample examined using the STXM are depicted in Fig. 8.

Carbon K-edge

The C K-edge image sequence was fit with protein, lipid and polysaccharide spectra (representing the major biomacromolecules commonly found in environmental samples), as well as carbonate and K (Dynes et al., 2006a). Threshold masking of these biomacromolecule component maps (not shown) revealed only a single organic carbon spectrum throughout the sample, which also contained peaks attributable to carbonate and K (Fig. 9A). Principal component analysis-cluster analysis of the C K-edge image sequence also indicated that the organic carbon in the sample is the same throughout. The main peaks in the organic carbon spectrum are due to carbonyl (288.5 eV) and ketone carbonyl (286.7 eV). Peaks due to carbonate (290.3 eV) and K (297.2 and 299.9 eV) are also apparent. The data thus indicates that the carbon in the skin is not related to proteins, lipids or polysaccharides.

In order to map the organic carbon, carbonate and K separately from each other, a modified carbon spectrum (referred to as "carbonyl") was made by subtracting a carbonate spectrum (i.e., calcite) from it and removing the K peaks (Fig. 9B). Two fittings were performed: one consisted of using calcium carbonate (i.e., calcite) and K (K_2CO_3 with carbonate signal subtracted) spectra, while the other used only a K_2CO_3 spectrum. Both fittings used the carbonyl spectrum and a slowly varying featureless signal (FS) (i.e., slightly decreasing line), which represents the inorganic components present in the sample.

269 The calcite and K spectra were published previously (Dynes et al., 2006a). This is the first time that
270 the K_2CO_3 spectrum has been published to our knowledge. It exhibits the spectral shape of carbonates
271 (Brandes et al., 2010). The component maps from the fittings are shown in Fig. 10. The carbonyl and
272 FS maps are similar for both fittings, thus, only those from the first fitting are shown. It is apparent that
273 the K_2CO_3 component map (Fig. 10D) is predominantly the sum of the carbonate and K component
274 maps. Overlay of the carbonate and K component maps revealed that there are at least two different
275 carbonate particles present: K_2CO_3 and another carbonate in the skin. In the sediment, only carbonates
276 were identified; neither organic carbon nor K was present (data not shown).

277 **Ca L-edge**

278 Previous work (Benzerara et al., 2004; Fleet and Liu, 2009) has shown that the energy positions of the
279 main Ca L-edge features are the same for the calcium carbonate polymorphs (e.g., calcite, aragonite,
280 vaterite) and dolomite ($CaMg(CO_3)_2$) occurring at 249.3 eV (Ca LIII-edge) and 252.6 eV (Ca LII-edge).
281 The number, energy positions, and relative intensities of the small peaks at lower energy relative to the
282 main features are dependent on the coordination, reflecting electronic and crystal-chemical details within
283 the first coordination sphere. Ca spectra derived from the image sequence from the skin and the sediment
284 are shown in Fig. 11E. The ratio of the peak at 351.4 eV and adjacent to the main peak at 352.6 eV in
285 the skin is 1.88. The ratio for the LII-edge peaks from the Ca in the sediment is 1.18. Hence, it appears
286 that the Ca in the sedimentary areas occurs as calcite and in the skin as vaterite (Benzerara et al., 2004).
287 However, potential spectral distortions associated with absorption saturation for optical density greater
288 than two are possible, and may have decreased the ratio of these peaks, particularly for the Ca in the
289 inorganic spectrum (Obst et al., 2009). Thus, it is possible that the $CaCO_3$ in the sediment is vaterite and
290 not calcite. Nevertheless, there is a small energy shift of the small peaks (Fig. 11F) from the skin and
291 sediment indicating that their coordination of Ca is slightly different. Two types of Ca compounds are
292 apparent when the Mg component map is overlaid with the Ca component maps (not shown); calcium
293 carbonate and either dolomite or calcium carbonate containing significant amounts of Mg.

294 The Ca speciation in the sediment surrounding (and away from) the skin was also examined. Spectral
295 fitting of the sediment Ca L-edge image sequence with the two spectra used in the skin/inorganic material
296 fitting, and subsequent threshold masking of these component maps indicated that results similar to those
297 for the skin were obtained, with regards to the ratio of the peaks. Thus it appears that absorption saturation
298 is likely the reason for some of the peak ratio difference. In any event, only one species of Ca is apparent
299 in the sediment, as the positions of the small peaks are the same between the two spectra. A Ca component
300 map (not shown) was generated using the result of a fitting with a calcite spectrum. Overlay of this
301 map with the carbonate component map from the C K-edge fitting showed that the Ca occurs as calcium
302 carbonate.

303 **Fe L-edge**

304 The oxidation state of Fe can be determined from the relative intensities of the double peaked Fe L3 signal
305 and from the position and number of peaks at the Fe L2-edge (Dynes et al., 2006b). The Fe L-edge image
306 sequence for the skin was fit using two Fe reference spectra (Fig. 12A), representing Fe(III) (goethite) and
307 Fe(II) (siderite) oxidation states and a featureless signal (FS) spectrum. The goethite and siderite spectra
308 were previously published (Dynes et al., 2015). The Fe(III) and Fe(II) component maps are shown in Figs.
309 12B and C, respectively. The Fe(III) and Fe(II) spectra (3-point smoothed) derived from the respective
310 component maps are characteristic of Fe(III) and Fe(II) spectra. The Fe(III) spectrum from the sample
311 also contains considerable Fe(II). The Fe L-edge image sequence of the sediment was fit with the goethite,
312 siderite and FS spectra. Threshold masking of these component maps indicated that there are Fe(II) and
313 Fe(III) species in the sediments. The Fe(II) species in the sediment is similar to that found in the skin,
314 whereas the Fe(III) species in the sediment contained more Fe(II) compared to that in the skin as evident
315 from the equal heights of the two peaks at the Fe L3-edge

316 Measurements of Al, Mg and Si K-edge were also performed and the data and discussions are provided
317 with the supplemental material (section 5).

318 **Carbonyl, Ca and Fe maps of a carbon-rich layer and its substructures at the SM beamline**

319 Phase-contrast optical microscopy (Fig. 13) on a 20 μm thick section of the skin revealed clearly-defined
320 layers in the region rich in carbon and carbonyl (as identified using the SM beamline).

321 Following the optical observations, the skin flake was again measured at the SM beamline in order to
322 identify the chemical state of the carbon associated with the optically-identified skin layers in Fig. 13.

Measurements of the area containing the skin were performed with photon beam of 280 eV (corresponding to an energy lower than the carbon K-edge energy), and 288.5 eV (carbonyl K-edge excitation energy) using photon absorption mode. The image collected at 280 eV was used for background subtraction in the computation of the image at 288.5 eV. Red in Fig. 14 represents carbonyl after background subtraction, while cyan represents the measurements at 280 eV (non-carbonyl).

The yellow rectangle encapsulates a region of the sample with a layered structure similar to those identified in Fig. 13. As Fig. 14 shows, this layer is rich in carbonyl, providing potential organic or organic-related material. The layers are clearly different both at chemical and morphological levels relative to other sedimentary regions of the sample.

A more detailed map of the area represented by the red rectangle in Fig. 14 was developed using a photon beam at 288.5 eV (carbonyl). This map is displayed in Fig. 15A. It shows potential carbonyl-rich substructures organized in a layer within the limits of the dinosaur skin. The existence of these substructures is reinforced by the evidence observed in both the optical and SEM images of the skin. The images captured using the three different techniques (X-ray SR, SEM and optical) all show similar geometrical features with apparent wave-like contours to the skin layers. These characteristics strongly suggest organized structures composed of subcircular substructures resembling cells. Artifacts introduced by the measurements can be discarded with high likelihood as it is unlikely that three completely different and independent techniques would randomly yield similar geometric features.

One of the substructures was mapped for carbon, Ca and Fe (Fig. 15B). As expected, the chemical states of these elements were found similar to those observed in section *Measurements using the SM Beamline Endstation* for the carbon-rich area (predominantly carbonyl, vaterite/calcite and goethite). As depicted in Fig. 15B, carbonyl is relatively uniformly distributed, while vaterite/calcium appears to delineate the substructure. More remarkably, goethite is highly concentrated at the center of this form. We have not investigated the reasons behind these distributions, and can only speculate about them at this point.

DISCUSSION

Measurements using the MidIR and SM beamlines have provided evidence of organic components in the mineralized skin. Both beamlines demonstrated that carbon in the carbonyl form is associated with the carbon-rich area observed with SEM measurements. The true nature and origin of such organic (or organic-related) matter could not be determined.

Measurements of an individual substructure in one of these layers (Fig. 15B) show conspicuous evidence apparently unrelated to random processes induced by diagenetic modifications, but rather, driven by the skin architecture. The associated organic material might, or might not, be original to the animal. In any case, the observed organic and inorganic materials are likely associated with the diagenetic processes that led to the preservation of the skin.

We also found that iron, in the form of FeCO_3 , is predominantly found at the center of one of these substructures forming the skin layers (Fig. 15B). These substructures closely resemble the geometry of skin cells that have been delineated and filled with vaterite/calcite.

It is also interesting to note that unlike previous suggestions where carbonate was implicate in the preservation of soft tissues (Manning et al., 2009), the skin layers reported here are predominantly associated with carbon in the form of carbonyl (Fig. 15A). Therefore, the conditions that led to the preservation of soft tissues in UALVP 53290 were likely very different from those reported by Manning et al. (2009). These conditions likely involved the early presence of kaolinite, which shrouded parts of the integument and provided an effective barrier to decay. Subsequent chemical reactions perhaps related to post-mortem bacterial activities (the organic material may be related to these activities), which is supported by the potential presence of anhydride acid (table 1 and associated discussions). Hence, it is reasonable to infer that a combination of factors including the presence of kaolinite, organic-related material, FeCO_3 and vaterite/calcite contributed to the preservation of epidermal layers in UALVP 53290.

In summary, following the identification of low Z regions in association with the epidermal scales (based on SEM analysis), several interesting features have been observed. Examinations based on correlation analysis between different peaks observed at the MidIR beamline provided further insight into the sample content. However, and based on the full dataset and results collected with the SM and MidIR beamlines, SEM and optical microscope, the message is that the sample contains a complex set of

compounds, with non-negligible evidence for the existence of organic-related material of some nature still associated with the epidermal scales.

The association of iron and kaolinite with the skin might indicate part of the diagenetic process involved in the preservation of this specimen. For example, kaolin might have accumulated over the surroundings of the animal after its death as part of the fossilization process. Assuming the darker areas in the thin-section consist of “fossilized” skin, we can speculate that the presence of kaolin might have produced an extrinsic barrier to decay and/or promoted the preservation of labile tissues. On the other hand, the abundance of iron in the oxidation state Fe(III) (goethite) was found to differ between the skin and associated sediments (see section *Fe L-edge*). The data collected with the SM beamline endstation supports a strong presence of goethite associated with the skin. As suggested by Schweitzer et al. (2013), iron in this state may play a role in the preservation of soft tissue by stabilizing and making it more likely to be preserved.

CONCLUSION

The main outcome of this work is the structural and compositional description of layers compatible with epidermal cell layers in the skin of a hadrosaur. These layers are composed of chains of carbon-rich subcircular bodies, predominantly in the form of carbonyl. Detailed analyses integrating different measurement techniques in synchrotron radiation, scanning electron microscopy and optical microscopy documented that calcite encapsulates these substructures, with iron (in the form of goethite) concentrated at its center. The source and distribution of iron in the substructures remains unclear, but which most likely played a role, along with vaterite/calcite, in the preservation of the micrometric structures.

The complex methodology applied in this study resulted in the following procedure:

1. fossilized skin tissue preserving carbon-rich layers were observed using scanning electron microscopy (SEM);
2. Measurements with synchrotron radiation in the mid-infrared (mid-IR) region of the spectrum revealed evidence of carbon in different organic forms, with carbonyl associated to the carbon-rich layers;
3. Synchrotron X-ray spectromicroscopy (SM) corroborated the previous observations by producing a map of the distribution of carbonyl. The distribution showed a strong correlation between carbonyl and the carbon-rich layers, establishing that carbon in the skin is predominantly of organic nature.
4. Optical microscopy along with SEM and SR images indicate that carbonyl layers are topologically organized and composed of smaller, subcircular substructures (Figs. 13, 4 and 15). The likelihood that these substructures are the product of geometrical or optical effects introduced in the measurements, or just random distributions, is minimized by the fact that the three techniques used are completely independent of each other, yet they returned similar results.

This study, thus, represents an attempt to combine different cutting-edge optical and chemical analyses. Future quantitative analysis and histological studies, however, should be directed towards addressing how these structures were preserved and how they compare to related extant analogues (e.g. crocodylians, birds).

ACKNOWLEDGMENTS

UALVP 5320 was discovered and prepared by PRB and Robin Sissons. We thank all the students and volunteers, especially Jeff Brewster for assistance collecting UALVP 53290. Grande Prairie Regional College, Eva Koppelhus (University of Alberta), Dick Barendregt and Certek Heat Machine are thanked for logistical assistance while in the field. We would also like to thank the Faculty of Science, University of Regina, for the financial support. PRB is funded by an Australian Research Council DECRA award (project ID: DE170101325)

REFERENCES

- Barbi, M., Tokaryk, T., and Tolhurst, T. (2014). Synchrotron radiation as a tool in paleontology. *Physics in Canada*, 70:8–12.

- Barrett, P. M., Evans, D. C., , and Campione, N. E. (2015). Evolution of dinosaur epidermal structures. *Biology Letters*, 11:20150229.
- Bell, P. (2012). Standardized terminology and potential taxonomic utility for hadrosaurid skin impressions: a case study for saurolophus from canada and mongolia. *PLoS ONE*, 7:e31295.
- Bell, P. and Campione, N. (2014). Taphonomy of the danek bonebed: a monodominant edmontosaurus (hadrosauridae) bonebed from the horseshoe canyon formation, alberta. *Canadian Journal of Earth Sciences*, 51:992–1006.
- Bell, P., Fanti, F., Acorn, J., and Sissons, R. (2013). Fossil mayfly larvae (ephemeroptera, cf. heptageniidae) from the late cretaceous wapiti formation, alberta, canada. *Journal of Paleontology*, 87:146–149.
- Bell, P., Fanti, F., Currie, P., and Arbour, V. (2014). A mummified duck-billed dinosaur with a soft-tissue cock's comb. *Current Biology*, 24:70–75.
- Bell, P. R. (2014). A review of hadrosaurid skin impressions. In Eberth, D. and Evans, D., editors, *The Hadrosaurs: Proceedings of the International Hadrosaur Symposium*, pages 572–590. Indiana University Press.
- Benzerara, K., Yoon, T. H., Tyliczszak, T., Constantz, B., Spormann, A. M., and Brown, G. E. (2004). Scanning transmission x-ray microscopy study of microbial calcification. *Geobiology*, 2:249–259.
- Bertazzo, S., Maidment, S., Kellepitis, C., Fearn, S., Stevens, M., and Xie, H. (2015). Fibres and cellular structures preserved in 75-million-year-old dinosaur specimens. *Nature Communications*, 6:7352.
- Brandes, J., Wirick, S., and Jacobsen, C. (2010). Carbon k-edge spectra of carbonate minerals. *Journal of Synchrotron Radiation*, 17:676–682.
- Coates, J. (2000). Interpretation of infrared spectra, a practical approach. In Meyers, R. A., editor, *Encyclopedia of Analytical Chemistry*, pages 10815–10837. John Wiley & Sons Ltd, Chichester.
- Davis, M. (2014). Census of dinosaur skin reveals lithology may not be the most important factor in increased preservation of hadrosaurid skin. *Acta Palaeontologica Polonica*, 59:601–605.
- Dynes, J., Lawrence, J., Korber, D., Swerhone, G., Leppard, G., and Hitchcock, A. (2006a). Quantitative mapping of chlorhexidine in natural river biofilms. *Science of the Total Environment*, 369:369–383.
- Dynes, J., Regier, T., Snape, I., Siciliano, S., and Peak, D. (2015). Validating the scalability of soft x-ray spectromicroscopy for quantitative soil ecology and biogeochemistry research. *Environmental Science & Technology*, 49:1035–1042.
- Dynes, J., Tyliczszak, T., Araki, T., Lawrence, J., Swerhone, G., Leppard, G., and Hitchcock, A. (2006b). Speciation and quantitative mapping of metal species in microbial biofilms using scanning transmission x-ray microscopy. *Environ. Sci. Technol.*, 40:1556–1565.
- Eberth, D., Shannon, M., and Noland, B. (2007). A bonebed database: classification, biases, and pattern of occurrence. In Rogers, R., Eberth, D., and Fiorillo, A., editors, *Bonebeds: Genesis, Analysis, and Paleobiological Significance*, pages 103–219. University of Chicago Press, Chicago.
- Fanti, F. (2009). Bentonite chemical features as a proxy of late cretaceous provenance changes: a case study from the western interior basin of canada. *Sedimentary Geology*, 217:112–127.
- Fanti, F., Bell, P., and Sissons, R. (2013). A diverse, high-latitude ichnofauna from the late cretaceous wapiti formation, alberta, canada. *Cretaceous Research*, 41:256–269.
- Fanti, F. and Catuneanu, O. (2009). Stratigraphy of the upper cretaceous wapiti formation, west-central alberta, canada. *Canadian Journal of Earth Sciences*, 46:263–286.
- Fanti, F. and Catuneanu, O. (2010). Fluvial sequence stratigraphy: the wapiti formation, west-central alberta, canada. *Journal of Sedimentary Research*, 80:320–338.
- Fanti, F. and Miyashita, T. (2009). A high latitude vertebrate fossil assemblage from the late cretaceous of west-central alberta, canada: evidence for dinosaur nesting and vertebrate latitudinal gradient. *Palaeogeography, Palaeoclimatology, Palaeoecology*, 275:37–53.
- Fleet, M. and Liu, X. (2009). Calcium l2,3-edge xanes of carbonates, carbonate apatite, and oldhamite (cas). *Am. Mineralog*, 94:1235–1241.
- Horner, J. R., Weishampel, D. B., and Forster, C. A. (2004). Hadrosauridae. In Weishampel, D. B., Dodson, P., and Osmólska, H., editors, *The Dinosauria*, pages 438–463. University of California Press, Berkeley.
- Kaznatcheev, K., Karunakaran, C., Lanke, U., Urquhart, S., Obst, M., and et al. (2007). Soft x-ray spectromicroscopy beamline at the csls: Commissioning results. *Nuclear Instruments and Methods in Physics Research A*, 582:96–99.
- Kellner, A. W. A. (1996). Fossilised theropod soft tissue. *Nature*, 379:32.

- 479 Lerotic, M., Jacobsen, C., Schäfer, T., and Vogt, S. (2004). Cluster analysis of soft x-ray spectromicroscopy
480 data. *Ultramicroscopy*, 100:35–37.
- 481 Li, Q., Gao, K.-Q., Meng, Q., Clarke, J., Shawkey, M., D’Alba, L., Pei, R., Ellison, M., Norell, M., and
482 Vinther, J. (2012). Reconstruction of microraptor and the evolution of iridescent plumage. *Science*,
483 335:1215–1219.
- 484 Li, Q., Gao, K.-Q., Vinther, J., Shawkey, M., Clarke, J., D’Alba, L., Meng, Q., Briggs, D., and Prum, R.
485 (2010). Plumage color patterns of an extinct dinosaur. *Science*, 327:1369–1372.
- 486 Lindgren, J., Sjövall, P., Carney, R., Uvdal, P., Gren, J., Dyke, G., Pagh Schultz, B., Shawkey, M., Barnes,
487 K., R., and Polcyn, M. (2014). Skin pigmentations provides evidence of convergent melanism in extinct
488 marine reptiles. *Nature*, 506:484–488.
- 489 Lindgren, J., Sjövall, P., Thiel, V., Zheng, W., Ito, S., Wakamatsu, K., Hauff, R., Kear, B. P., Engdahl,
490 A., Alwmark, C., Eriksson, M. E., Jarenmark, M., Sachs, S., Ahlberg, P. E., Marone, F., Kuriyama,
491 T., Gustafsson, O., Malmberg, P., Thomen, A., Rodríguez-Meizoso, I., Uvdal, P., Ojika, M., and
492 Schweitzer, M. H. (2018). Soft-tissue evidence for homeothermy and crypsis in a jurassic ichthyosaur.
493 *Nature*, 564:359–365.
- 494 Lingham-Soliar, T. (2008). A unique cross-section through the skin of the dinosaur psittacosaurus from
495 china showing a complex fibre architecture. *Proceedings of the Royal Society B*, 275:775–780.
- 496 Manning, P., Morris, P., McMahon, A., Jones, E., Gize, A., Macquaker, J., Wolff, G., Thompson, A.,
497 Marshall, J., Taylor, K., Lyson, T., Gaskell, S., Reamtong, O., Sellers, W., van Dongen, B., Buckley, M.,
498 and Wogelius, R. (2009). Mineralized soft-tissue structure and chemistry in a mummified hadrosaur
499 from the hell creek formation. *Proceedings of the Royal Society B*, 276:3429–3437.
- 500 Martill, D. M. (1991). Organically preserved dinosaur skin: taphonomic and biological implications.
501 *Modern Geology*, 16:61–68.
- 502 May, T., Ellis, T., and Reininger, R. (2007). Mid-infrared spectromicroscopy beamline at the canadian
503 light source. *Nuclear Instruments and Methods in Physics Research A*, 582(1):111–113.
- 504 McIntyre, N. S., Sherry, N., Fuller, M. S., Feng, R., Kotzer, T., and et al. (2010). X-ray fluorescence
505 spectroscopy and mapping using excitation from white and broad bandpass synchrotron radiation.
506 *Journal of Analytical Atomic Spectrometry*, 25:1381–1389.
- 507 Obst, M., Dynes, J., Lawrence, J., Swerhone, G., Benzerara, K., Karunakaran, C., Kaznatcheev, K.,
508 Tyliczszak, T., and Hitchcock, A. (2009). Precipitation of amorphous CaCO_3 (aragonite-like) by
509 cyanobacteria: A stxm study of the influence of eps on the nucleation process. *Geochim. Cosmochim*
510 *Acta*, 73:4180–4198.
- 511 Osborn, H. F. (1912). Integument of the iguanodont dinosaur trachodon. *Memoirs of the American*
512 *Museum of Natural History*, 2:33–54.
- 513 Schweitzer, M., Wittmeyer, J., Horner, J., and Toporski, J. (2005). Soft-tissue vessels and cellular
514 preservation in tyrannosaurus rex. *Science*, 307:1952–1955.
- 515 Schweitzer, M., Zheng, W., Cleland, T., Goodwin, M., Boatman, E., Theil, E., Marcus, M., and Fakra, S.
516 (2013). A role for iron and oxygen chemistry in preserving soft tissues, cells and molecules from deep
517 time. *Proc Biol Sci.*, 281(1775):20132741.
- 518 Sternberg, C. M. (1953). A new hadrosaur from the oldman formation of alberta: Discussion of
519 nomenclature. *Canadian Department of Resource Development Bulletin*, 128:1–12.
- 520 Zhang, F., Kearns, S., Orr, P., Benton, M., Zhou, Z., Johnson, D., Xu, X., and Wang, X. (2010). Fossilized
521 melanosomes and the colour of cretaceous dinosaurs and birds. *Nature*, 463:1075–1078.

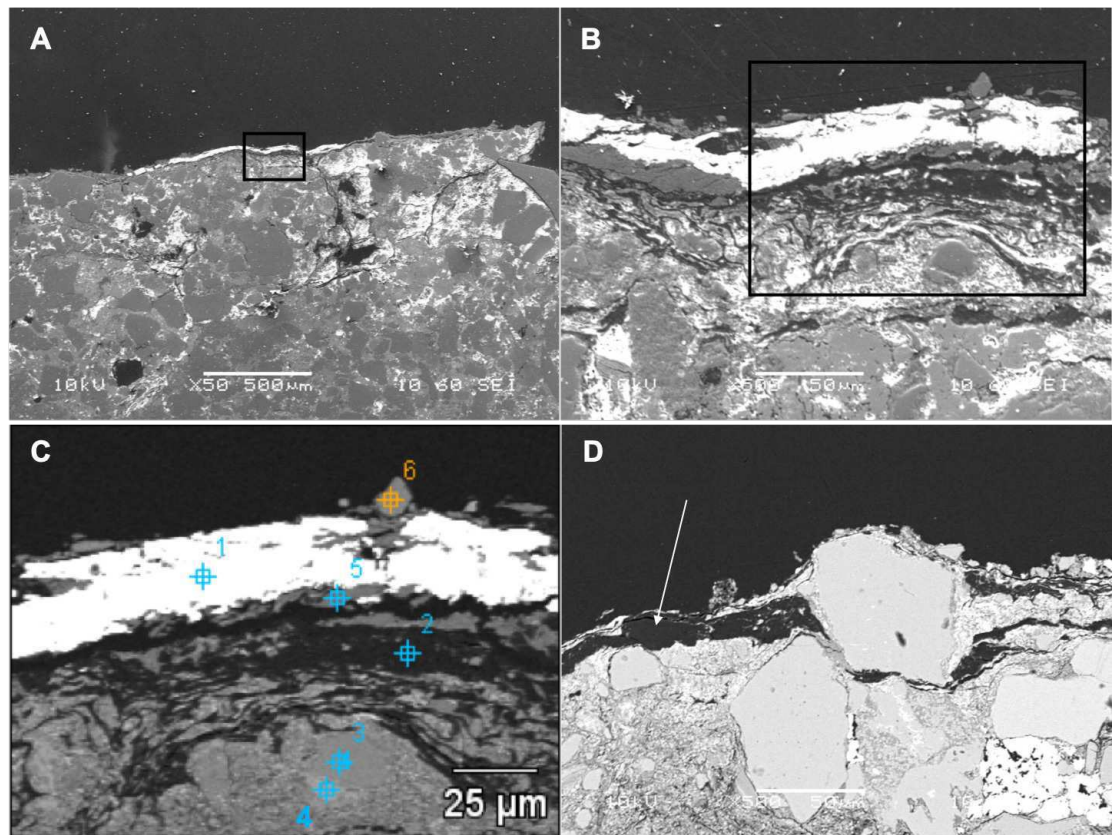


Figure 2. SEM images from a sample of the skin from UALVP 53290 using (A,B) secondary electron (SEI), and (C,D) back-scattered electron filters. (A) Cross-section representing the epidermal scale and underlying matrix (scale = 500 μm). Sedimentary deposits (e.g. individual sand grains) are dominant in this image. (B) A magnified image of the boxed area shown in (A) (scale = 50 μm). The white top layer is of sedimentary nature (more details further below) and partially covers the top of several epidermal scales. A thin darker area under this white surface and above another sedimentary region can also be observed. (C) Close up of boxed region in (B) (scale = 25 μm) imaged using BSE. Brighter areas represent higher atomic number (Z) elements. Richer carbon-based (lower Z) structures are expected to show as darker areas, such as the one just under the top white layer in this image. Numbers and cross-hairs indicate specific points where spectral distributions were obtained using X-ray emission spectroscopy. (D) BSE image showing a discrete darker zone (low Z; indicated with an arrow) close to the top of the sample (scale = 50 μm).

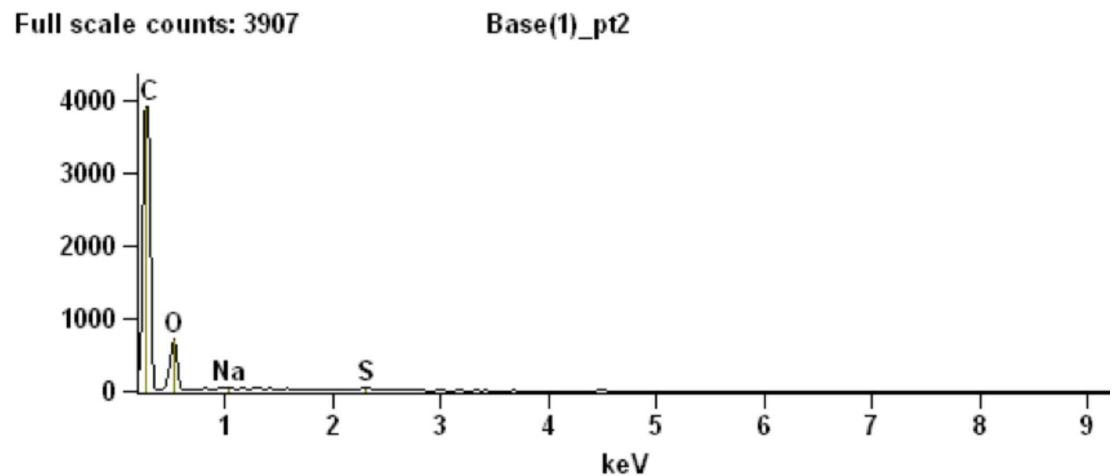


Figure 3. SEM chemical analysis for point 2 in Fig 2C showing high carbon content typical of the dark (low Z) regions identified by BSE SEM.

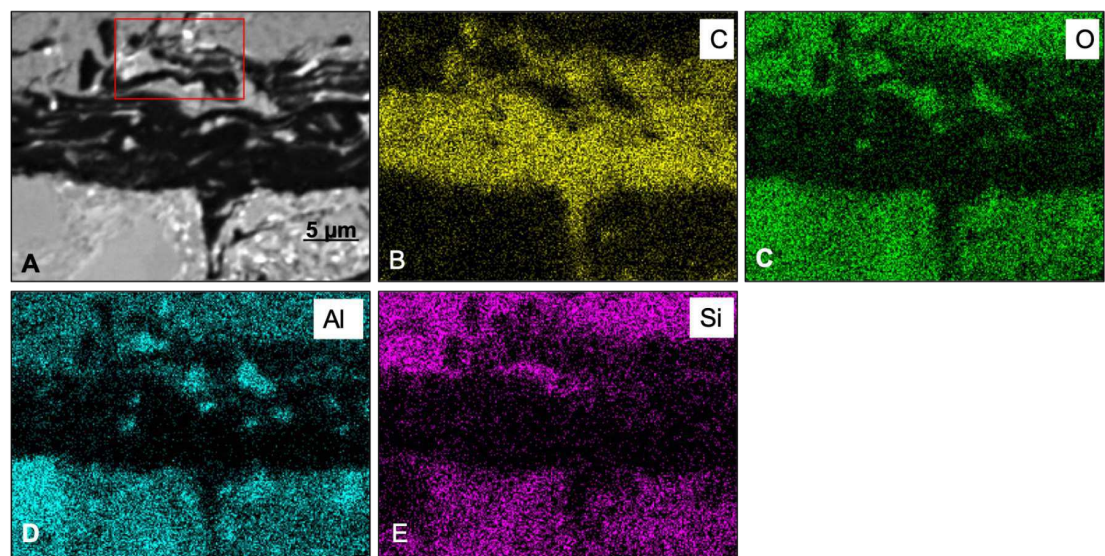


Figure 4. SEM elemental maps for Carbon (B), Oxygen (C), Aluminum (D) and Silica (E) of a region containing a carbon-rich area and sediments. The maps show a clear correlation between the darker area in the map (A) and the carbon distribution in the sample. Boxed area in (A) shows an apparent chain of sub-structures. The scale bar is 5 μ m for all figures.

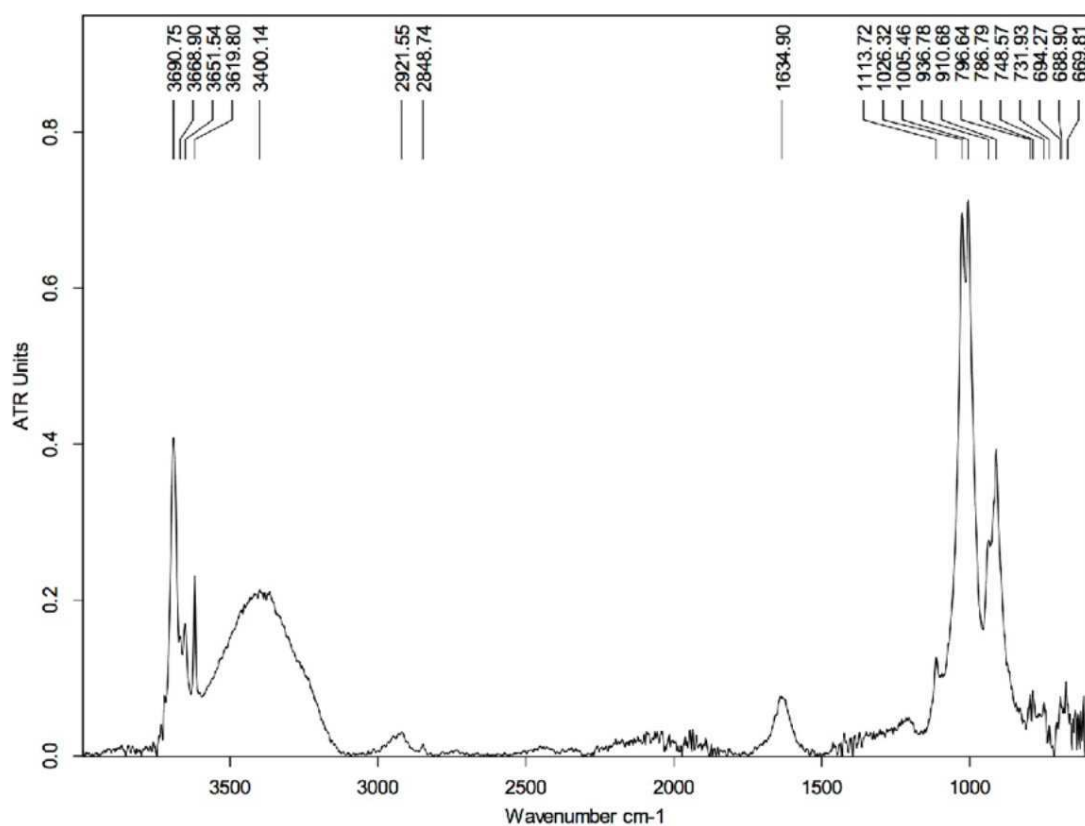


Figure 5. FTIR spectrum of the HCl-treated skin sample collected using Attenuated Total Reflectance (ATR) in absorption mode. The peaks at 3690, 3651, 3619, 1113, 1026, 1005, 936, and 910 cm⁻¹ are characteristics of kaolinite.

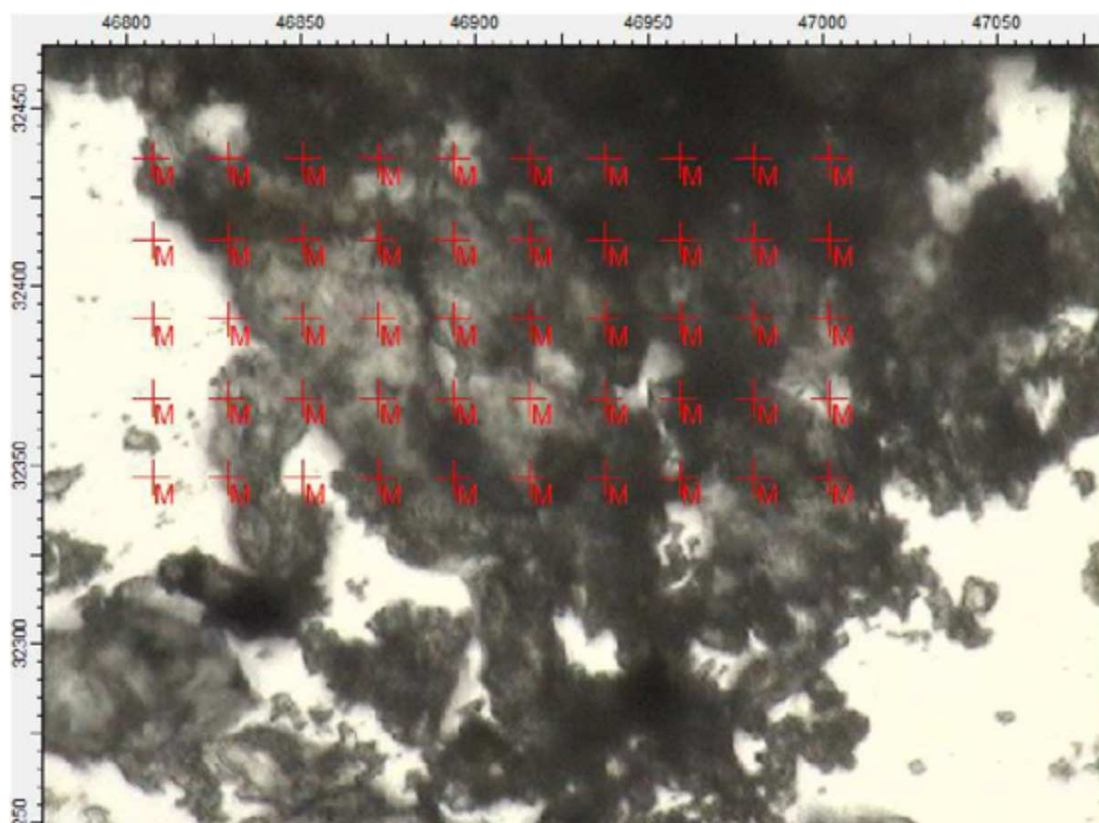


Figure 6. Region of the darker powder sample mapped using FTIR in transmission mode. Each cross on the map represents a position used to collect a spectrum.

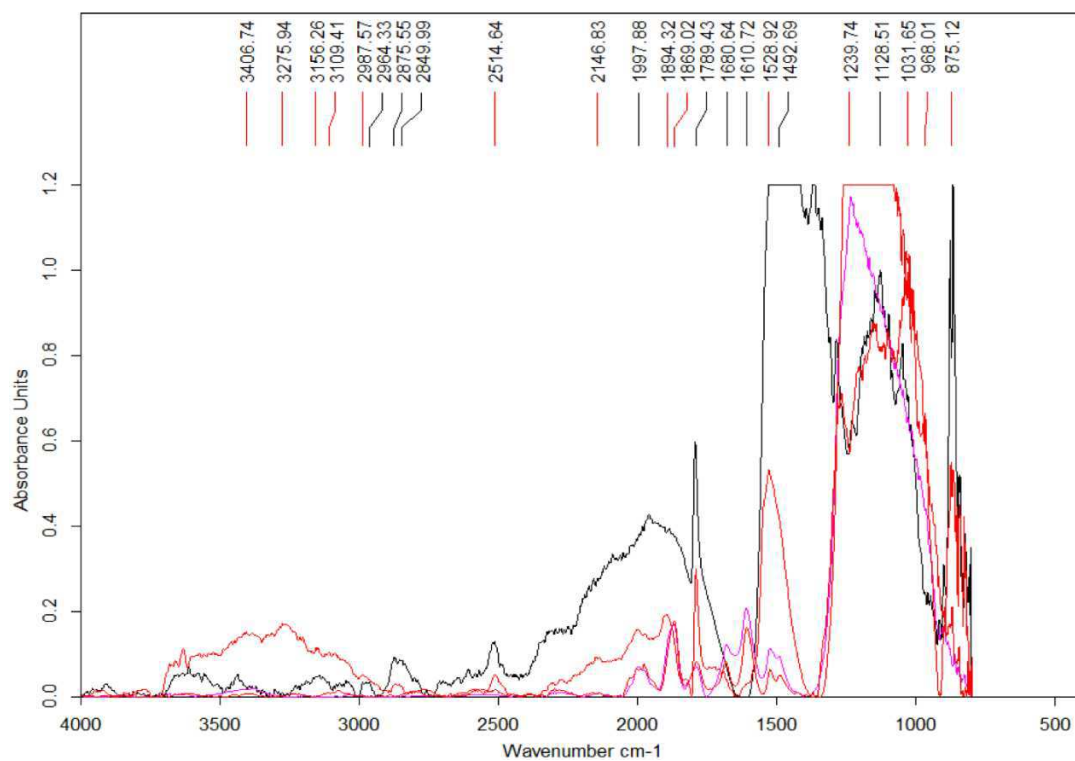


Figure 7. Select set of spectra extracted from the map in Fig. 6 using FTIR in transmission mode.

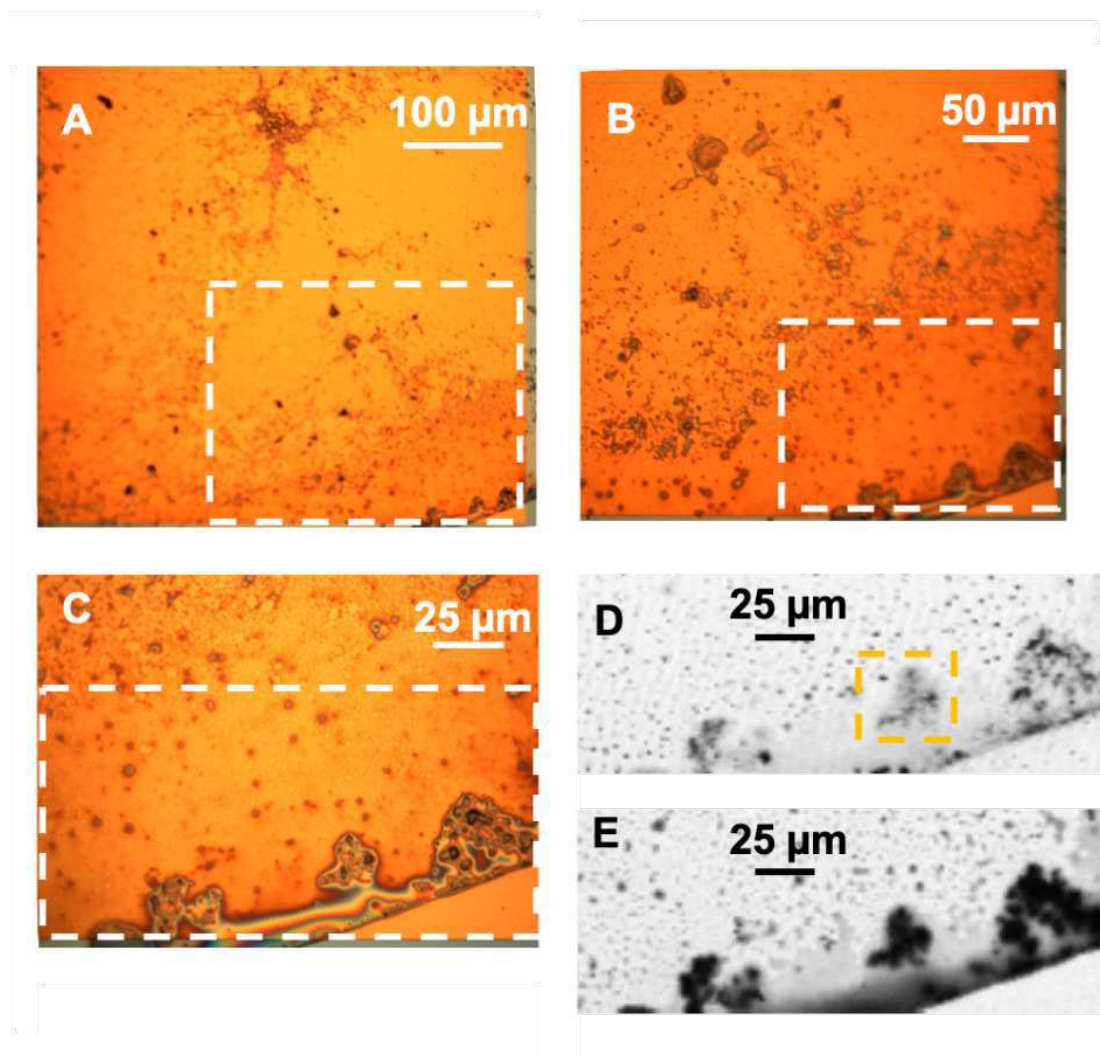


Figure 8. (A-C) Optical images of the hadrosaur skin and sediment debris from the microtome. The white rectangles show the region magnified in each successive image. (D) Transmission image at 280 eV of the boxed region in C, showing the inorganic material. The yellow rectangle shows the area studied in detail using STXM and depicted in Fig. 10. (E) Transmission image at 300 eV of the same area, showing the organic material.

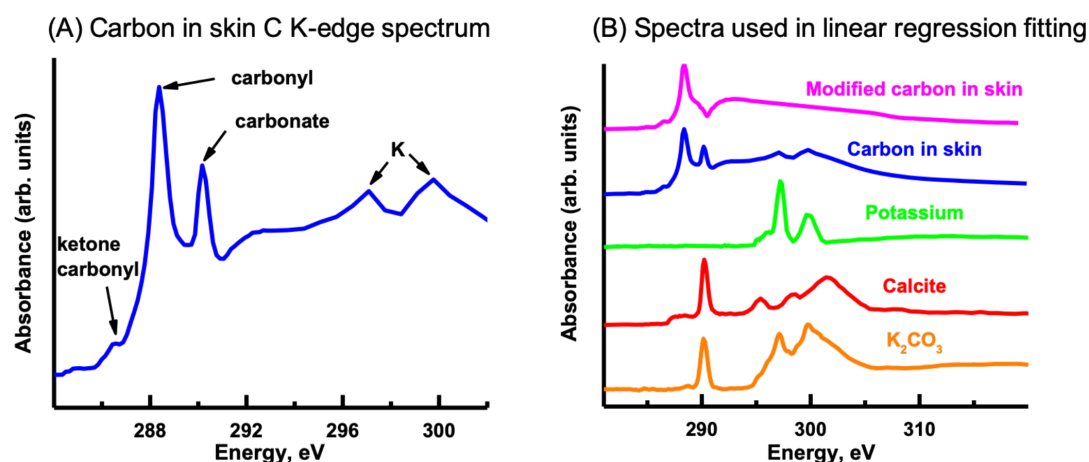


Figure 9. Carbon K-edge XANES reference spectra used in the initial linear regression fitting of the carbon image sequence and the organic carbon spectrum derived from the skin. (A) Carbon spectrum derived from the skin using PCA-CA. Only one carbon spectrum is evident throughout the skin, consisting of peaks attributed to ketone carbonyl (286.7 eV), carbonyl (288.5 eV), carbonate (290.3 eV) and K (297.2, 299.9 eV). (B) To distinguish the organic carbon from the carbonate and K in the skin, the carbonate (calcite; red spectrum) and K peaks (green) were removed, resulting in a modified carbon in the skin spectrum (pink). To separate the carbonate from the K, the K₂CO₃ spectrum was modified by subtracting a calcium carbonate (CaCO₃) spectrum from it. See text for details.

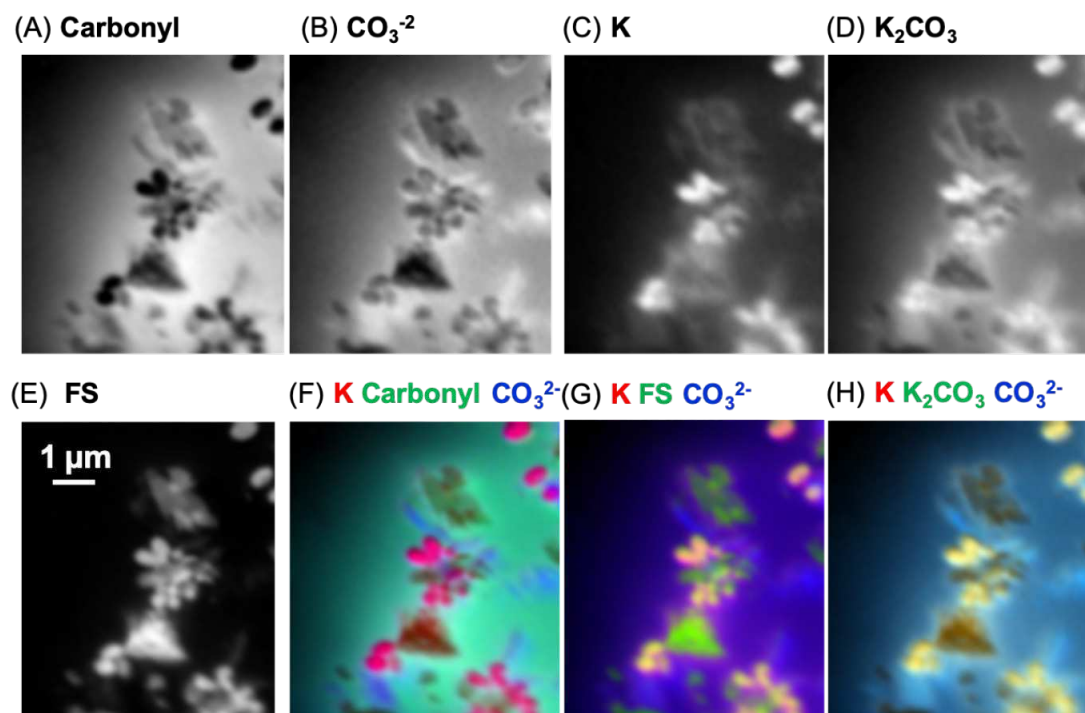


Figure 10. Carbon component maps of the area shown in Fig. 8E derived from the linear regression fitting of a C K-edge image sequence using reference spectra and the modified carbon ("carbonyl") spectrum (see Fig. 9B). (A) Carbonyl, (B) carbonate (CO_3^{2-}), (C) K, (D) K_2CO_3 , and (E) featureless signal (FS). Two fittings were carried out; the first fitting used the modified carbon from skin spectrum, and the carbonate and K spectra. The second fitting used the K_2CO_3 instead of the K and carbonate spectra. Both fittings used the same slow varying featureless signal. The carbonyl and FS maps were similar for both fittings, thus, only those from the first fitting are shown. Color composites of selected component maps. (F) K = red; carbonyl = green; carbonate = blue; (G) K = red; FS = green; carbonate = blue; (H) K = red; K_2CO_3 = green; CO_3^{2-} = blue.

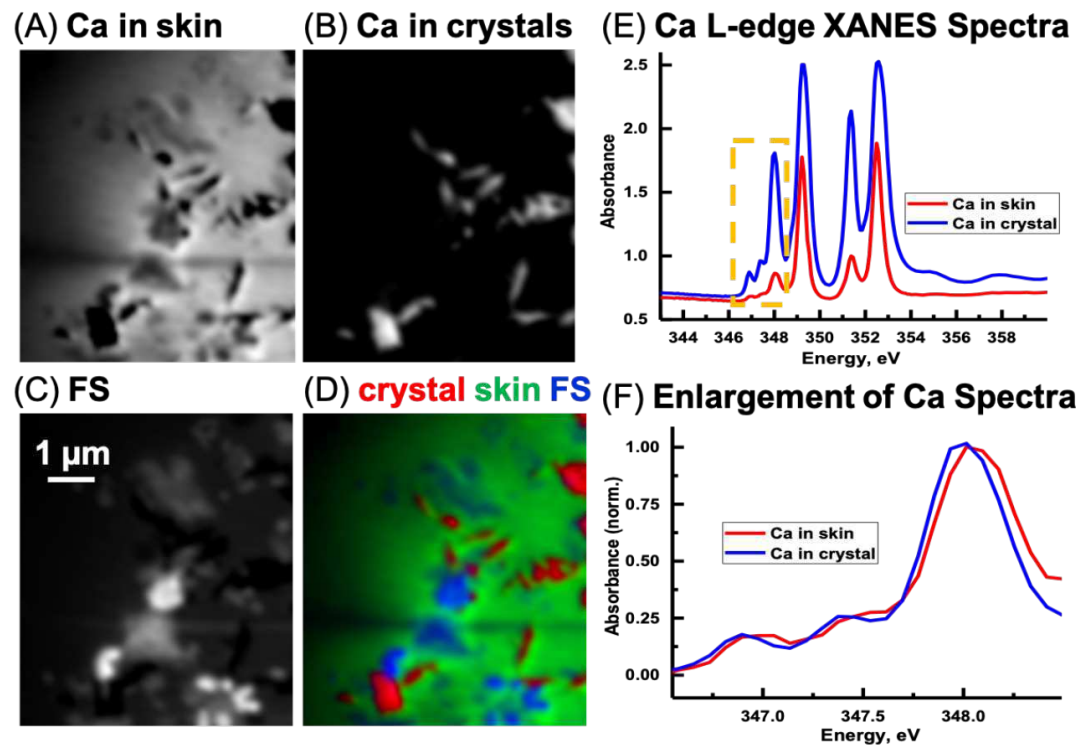


Figure 11. Calcium component maps derived from the linear regression fitting of a Ca L-edge image sequence using spectra derived from the Ca in the skin and in the inorganic particles (crystal) found associated with the integument. (A) Ca in skin, (B) Ca in crystals, and (C) featureless signal (FS). (D) Color composites of the component maps (Ca in crystal = red, Ca in skin = green and slow varying featureless signal (FS) = blue). (E) Ca L-edge XANES spectra derived by threshold masking of the pixels (not shown) from the inorganic particles and from the skin component maps, (F) The spectra from the yellow box in (E) was enlarged and normalized on the 348 eV peak to better show the differences in peak position between the skin and inorganic spectra.

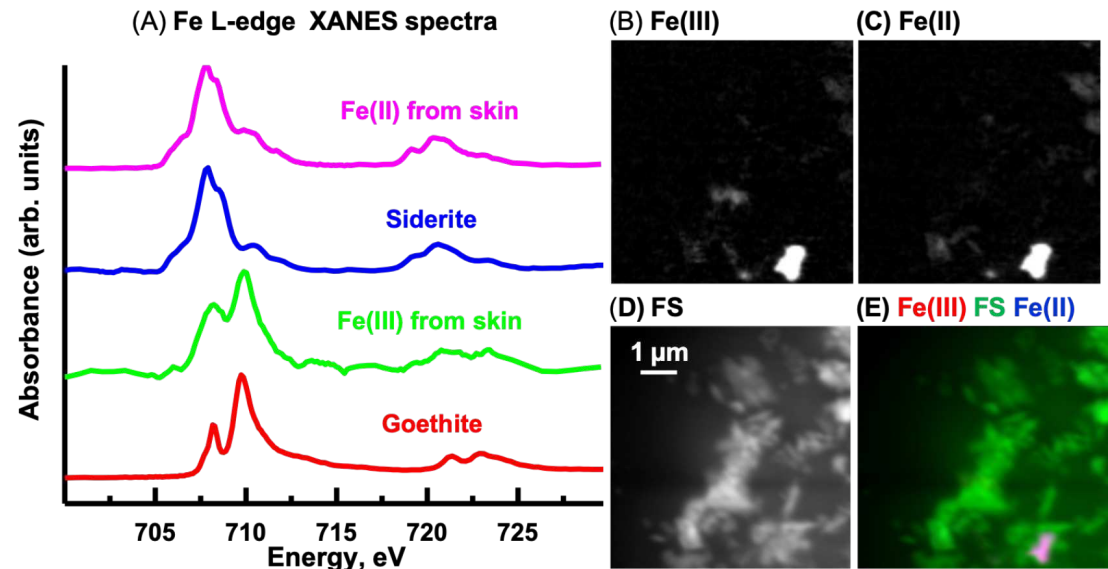


Figure 12. Iron component maps derived from the linear regression fitting of a Fe L-edge image sequence using reference spectra. (A) Comparison of Fe(III) and Fe(II) spectra derived by threshold masking of the component maps to the siderite (Fe(II)) and goethite (Fe(III)) reference spectra. Component maps: (B) Fe(III), (C) Fe(II) and (D) slow varying featureless signal (FS). (E) Color composites of the component maps (Fe(III) = red; featureless signal = green; Fe(II) = blue).

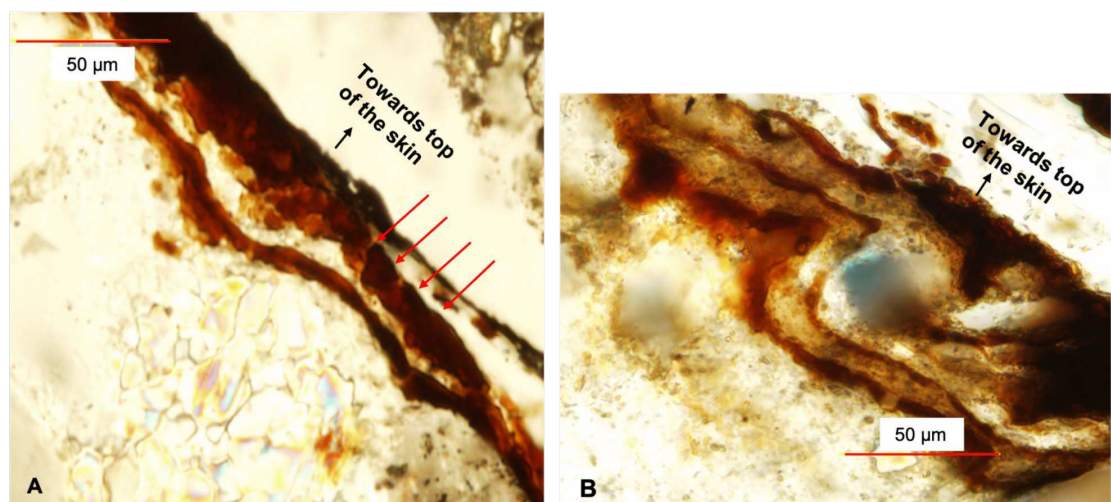


Figure 13. Optical images of the integumentary features of the skin of UALVP 53290 showing layered arrangement apparently composed of smaller substructures as visible in (A) (red arrows). (B) The layers frange in thickness from 10 – 15 μm to as thick as 50 – 100 μm (not shown).

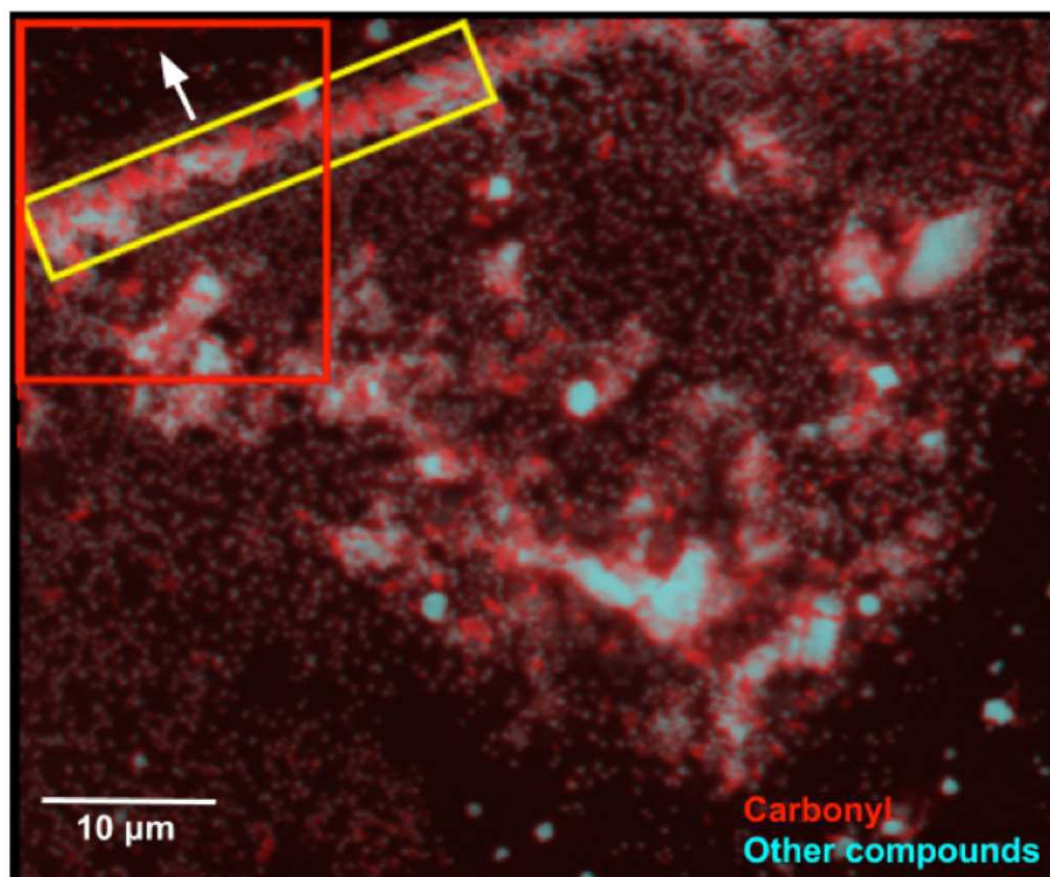


Figure 14. Distribution of carbonyl (red) compared to the distribution of other compounds (cyan) in a $65 \times 50 \mu\text{m}$ area of the sample. This area was measured in $0.1 \mu\text{m}$ steps. A layer of skin, identified by the yellow rectangle and predominantly composed of carbonyl, can be seen diagonally at the top-left corner of the image. The white arrow points towards the top of the skin. The red box represents the area detailed in Fig. 15.

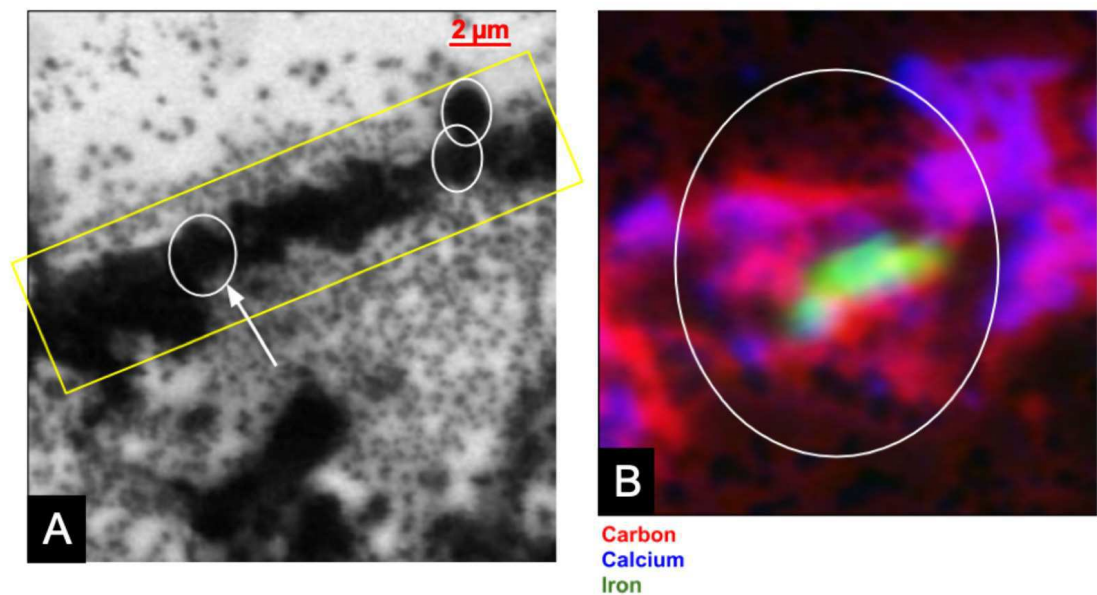


Figure 15. (a) Carbonyl (288.5 eV) map of the area within the red rectangle depicted in Fig. 14. The map covers an area of 20 x 20 μm of the sample in steps of 0.1 μm . The scale bar is 2 μm . Dark areas correspond to the presence of carbonyl (the data were collected with the detector in X-ray absorption mode). The yellow rectangle highlights a carbonyl layer which seems to be organized in smaller substructures, with three of them delineated by the white circles. (b) Elemental mapping of carbon (red), calcium (blue) and iron (green) of one of the substructures indicated by the white arrow in Fig. 15.